Nonlinear Hall Effect from Long-Lived Valley-Polarizing Relaxons

Jae-Mo Lihm[*] and Cheol-Hwan Park[†]
Department of Physics and Astronomy, Seoul National University, Seoul 08826, Korea;
Center for Correlated Electron Systems, Institute for Basic Science, Seoul 08826, Korea;
and Center for Theoretical Physics, Seoul National University, Seoul 08826, Korea

(Received 11 September 2023; revised 7 December 2023; accepted 9 January 2024; published 8 March 2024)

The nonlinear Hall effect has attracted much attention due to the famous, widely adopted interpretation in terms of the Berry curvature dipole in momentum space. Using *ab initio* Boltzmann transport equations, we find a 60% enhancement in the nonlinear Hall effect of n-doped GeTe and its noticeable frequency dependence, qualitatively different from the predictions based on the Berry curvature dipole. The origin of these differences is long-lived valley polarization in the electron distribution arising from electron-phonon scattering. Our findings await immediate experimental confirmation.

DOI: 10.1103/PhysRevLett.132.106402

The nonlinear Hall (NLH) effect [1–8] is a nonlinear analog of the Hall effect that describes a transverse current response to two electric fields. Unlike its linear counterpart, the NLH effect occurs even in nonmagnetic systems without an external magnetic field. The NLH effect is attracting much attention due to its close connection to an intrinsic geometric property of the electronic structure [2,9]. Applications such as probing electronic topology [10], radio-frequency rectification [11], and terahertz photodetection [12–14] are under active investigation.

The standard interpretation of the intrinsic NLH effect attributes the effect to the momentum-space dipole of the Berry curvature [1,2,9] [Fig. 1(a)]. This "Berry curvature dipole" picture underlies many experimental [4,5,8] and theoretical [3,10,14] studies of the NLH effect. An assumption key to this interpretation is the constant relaxation time approximation (CRTA). In this approximation, both the NLH conductivity and the linear conductivity are proportional to the relaxation time, a phenomenological constant, with the prefactors being the Berry curvature dipole and the Drude weight, respectively. The ratio between the two conductivities, which determines the current responsivity, the figure of merit for rectification from the NLH effect [12], has been considered a purely intrinsic quantity determined only by the electronic structure [14].

In real systems, however, scattering does not simply relax the driven carriers to the equilibrium as assumed in the CRTA; its microscopic detail determines the nonequilibrium distribution of the carriers. Consequently, CRTA breaks the conservation of total charge [15] and completely misses the emergent quasiconservation of quantities such as total momentum [16–18], which manifests as enhanced lifetimes of such quantities. For example, CRTA does not distinguish forward and backward scatterings, even though only the latter dissipate electric current and contribute to the momentum lifetime [16]. The disparate timescales of the dynamics can be captured only by solving the full Boltzmann transport equation (BTE) which takes into account vertex corrections to the conductivity [19]. Many studies have reported significant vertex corrections to linear transport properties, including the linear magnetoresistance [20] and the linear anomalous Hall effect [21] of the Rashba Hamiltonian, and the linear mobility [22–27] and spin lifetimes [28,29] of real materials under electron-phonon scattering. However, it is still unclear to what extent and through which long-lived quantity vertex correction affects the intrinsic NLH effect.

To gain a physical understanding of the nature of the vertex correction, one can use the relaxon method [30,31]. Relaxons are normal modes of the dynamics described by BTE with well-defined lifetimes. The relaxon method has been applied to study the quasiconservation of the total momentum of phonons [31,32]. However, for electronic transport, quantities other than the total momentum may

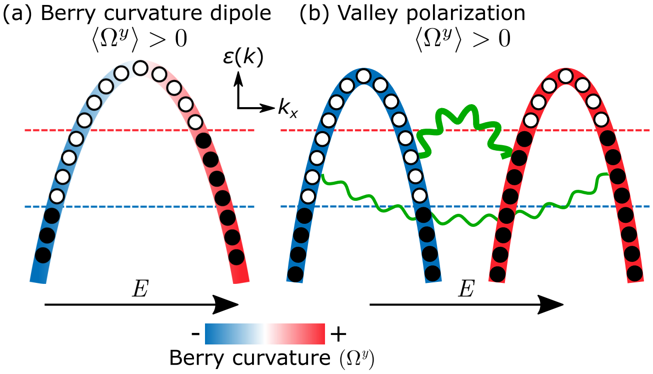

FIG. 1. Mechanisms of the intrinsic NLH effect. (a) Berry curvature dipole, and (b) scattering-induced valley polarization. The thickness of the wiggles represents the strength of the scattering.

become long-lived. Whether the relaxon method could be utilized for electronic systems to investigate long-lived quantities remains an open question. Although the electron relaxon method was used to compute the linear conductivity [33], it has not been used for the NLH conductivity, and, much more importantly, neither the analysis of each relaxon mode and its the contribution to the linear or NLH conductivity nor the physical intuition we obtain therefrom has been reported.

In this Letter, we report a large contribution to the intrinsic NLH effect that is not captured by the Berry curvature dipole picture. By exactly solving the linearized BTE for hole-doped GeTe, we find that the current responsivity is up to 60% larger than that predicted by the CRTA, and exhibits a sharp frequency dependence. To uncover the origin of these results, we develop a theory of electronic relaxons and find a novel structure in their eigenspectrum and eigenstates. Based on the relaxon analysis, we attribute the enhancement and frequency dependence to a long-lived difference in the carrier population between the valleys or the minivalleys [Fig. 1(b)].

The BTE describes the time evolution of the electron occupation at time t. We write $f_i(t) = f_i^{(0)} + \delta f_i(t)$, where $f_i^{(0)}$ is the equilibrium Fermi-Dirac occupation in the absence of the external electric field and i the electron eigenstate index specifying both the band and the momentum. In the linear response regime for a uniform, monochromatic electric field $\mathbf{E}(t) = \mathrm{Re}\mathbf{E}e^{i\omega t}$, the BTE reads as [16]

$$\begin{aligned} \delta f_i(t) &= \mathrm{Re}\sum_{b=x,y,z} E^b \delta f_i^b(\omega) e^{i\omega t}, \\ i\omega \delta f_i^b(\omega) &= e\, v_i^b f_i^{(0)\prime} - \sum_j S_{ij} \delta f_j^b(\omega). \end{aligned} \tag{1}$$

Here, $-e$ is the electron charge, v_i^b the band velocity, $f_i^{(0)\prime}$ the energy derivative of the Fermi-Dirac distribution, and S the scattering matrix [Eq. (A2)]. Setting $\omega = 0$ gives the dc BTE. The diagonal part of the scattering matrix is the inverse of the single-particle lifetime: $S_{ii} = \tau_i^{-1}$. In the CRTA, S is approximated to be proportional to the identity matrix, $S_{ij}^{\mathrm{CRTA}} = \tau^{-1}\delta_{ij}$, where the inverse lifetime τ^{-1} is a free parameter. In this work, we focus on the electron-phonon scattering [24,34].

From the solution of the BTE, one can compute the linear and nonlinear conductivities as

$$\begin{aligned} \sigma_{\mathrm{L}}^{ab}(\omega) &= -\frac{e}{V_{\mathrm{cell}} N_k} \sum_i v_i^a \delta f_i^b(\omega), \\ \sigma_{\mathrm{NLH}}^{a;bc}(\omega) &= \frac{e^2}{2\hbar V_{\mathrm{cell}} N_k} \sum_d \epsilon_{adc} \sum_i \Omega_i^d \delta f_i^b(\omega), \end{aligned} \tag{2}$$

where a, b, c, and d are Cartesian indices, Ω_i^d the band Berry curvature, ϵ_{acd} the Levi-Civita symbol, V_{cell} the volume of the unit cell, and N_k the number of k points in the full k-point grid. (See Secs. A and F of the Supplemental Material for details of the BTE formalism and computational details, respectively [35]).

We study the linear and nonlinear conductivities of p-doped α-GeTe, a ferroelectric semiconductor with a large Rashba-type band splitting [60]. Below the transition temperature of 720 K, the Te atom shifts along the [111] direction, which we choose to be the z axis, creating a nonzero polarization. The broken inversion symmetry allows the NLH response, and GeTe has been proposed as a candidate material for terahertz photodetection using the NLH effect [14]. GeTe is typically heavily p doped due to the thermodynamically favorable Ge vacancies [61]. Hole concentrations as low as 5×10^{19} cm^{-3} or below have been realized by additional doping [62–64]. Doping was treated using the rigid-band approximation, and the free-carrier screening to electron-phonon coupling was included [65].

We consider the in-plane linear conductivity σ_{L}^{xx} and the $\sigma_{\mathrm{NLH}}^{z;xx}$ component of the NLH conductivity, unless otherwise stated (see Fig. S1 for the crystal structure and the field and current directions). The linear conductivity is isotropic along the in-plane directions: $\sigma_{\mathrm{L}}^{xx} = \sigma_{\mathrm{L}}^{yy} \neq \sigma_{\mathrm{L}}^{zz}$. All nonzero components of the NLH conductivity are related by symmetry: $\sigma_{\mathrm{NLH}}^{z;xx} = \sigma_{\mathrm{NLH}}^{z;yy} = -\sigma_{\mathrm{NLH}}^{x;xz} = -\sigma_{\mathrm{NLH}}^{y;yz}$. We focus on the current responsivity, the figure of merit for terahertz rectification [12]. For a sample with size $L_x \times L_y \times L_z$, the current responsivity R is [12]

$$R = \frac{J_{\mathrm{NLH}}^z L_x L_y}{J_{\mathrm{L}}^x E^x L_x L_y L_z} = \frac{1}{L_z} \frac{\sigma_{\mathrm{NLH}}^{z;xx}}{\sigma_{\mathrm{L}}^{xx}}. \tag{3}$$

Figure 2(a) shows that for a wide range of carrier densities, the current responsivity calculated with BTE is considerably larger than that obtained in the CRTA. Figure 2(b) shows that the ac responsivity in the terahertz regime is sharply peaked at zero frequency and rapidly

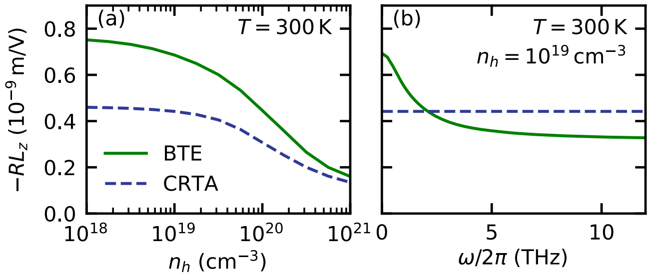

FIG. 2. (a) Hole-density dependence, and (b) frequency dependence of the current responsivity multiplied by the sample length L_z for GeTe, which equals the ratio of the NLH conductivity to the linear conductivity [Eq. (3)]. All the results shown in this and the following figures were obtained at hole density $n_h = 10^{19}$ cm^{-3} and temperature $T = 300$ K unless otherwise noted.

drops at higher frequencies, while the responsivity in the CRTA is frequency independent. In Sec. C of the Supplemental Material [35], we show that this feature is present for a wide range of temperatures. These findings demonstrate a substantial vertex correction to the NLH effect, and suggest that an important mechanism for the intrinsic NLH effect beyond the conventional Berry curvature dipole picture exists.

To uncover the mechanism underlying the large increase and frequency dependence of the NLH conductivity, we generalize the relaxon decomposition, originally developed for phonon transport [30,31], to the case of electrons. Relaxons are normal modes of the BTE, which can be obtained via the eigenmodes of the scattering matrix S. Since S is not symmetric, one first defines the symmetrized scattering matrix $\tilde{S}$ by applying a similarity transformation [33]:

$$\tilde{S}_{ij} = S_{ij}\sqrt{\frac{f_j^{(0)}\left(1-f_j^{(0)}\right)}{f_i^{(0)}\left(1-f_i^{(0)}\right)}}. \tag{4}$$

This matrix is real valued, symmetric, and positive semidefinite, and has the same set of eigenvalues as S. (We note that other types of symmetric scattering matrices, which are *not* related to S by similarity transformations, have also been used [66–68].) We diagonalize $\tilde{S}$ as

$$\sum_j \tilde{S}_{ij}\Theta_{jp} = \Gamma_p \Theta_{ip}, \tag{5}$$

with the normalization condition $(\Theta^\intercal\Theta)_{pp'} = V_{\text{cell}} N_k \delta_{pp'}$. Each column Θ_{ip} describes a relaxon mode whose relaxation rate or inverse lifetime is Γ_p. Each eigenvalue Γ_p^{-1} is a non-negative, physical lifetime of a collective mode. One of the relaxons has a zero eigenvalue and corresponds to the change of the chemical potential [Eq. (A21)]; the remaining relaxons have positive eigenvalues.

By writing the stationary-state electron distribution in the relaxon basis, one can decompose the conductivities into the contributions of individual relaxons:

$$\begin{aligned} \text{Re}\sigma_{\text{L}}^{ab}(\omega) &= e^2\kappa \sum_p \tilde{v}_p^a \tilde{v}_p^b \frac{\Gamma_p}{\Gamma_p^2+\omega^2}, \\ \text{Re}\sigma_{\text{NLH}}^{a;bc}(\omega) &= -\frac{e^3\kappa}{2\hbar}\sum_d \epsilon_{adc} \sum_p \tilde{\Omega}_p^d \tilde{v}_p^b \frac{\Gamma_p}{\Gamma_p^2+\omega^2}. \end{aligned} \tag{6}$$

Here, κ is the charge compressibility, and $\tilde{v}_p^a$ and $\tilde{\Omega}_p^a$ are the effective velocity and Berry curvature of the relaxons, respectively, which are the averages of the quantities over the electron eigenstates weighted by the relaxon eigenvector [Eqs. (A24) and (A25)]. The charge compressibility can be understood as the charge carried by a single relaxon, which is a collective excitation spanning the whole Fermi surface. For heat transport by phonon relaxons, the charge compressibility is replaced with the heat capacity [31].

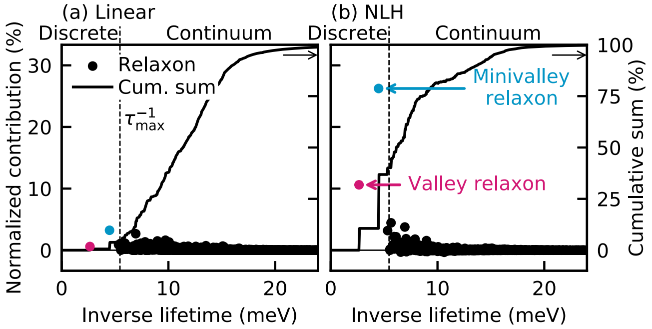

FIG. 3. Relaxon decomposition of the (a) linear conductivity and (b) NLH conductivity of GeTe. We only show individual contributions whose absolute value is greater than 10^{-3}%.

Figure 3 shows the contribution of each relaxon to the linear and NLH conductivities. The relaxon spectrum has two parts, discrete levels and a continuum, separated by the inverse of $\tau_{\text{max}} = \max_i \tau_i$, the longest single-particle lifetime. Relaxons with lifetimes longer than τ_{max} ($\Gamma_p^{-1} > \tau_{\text{max}}$) display a discrete spectrum, while those with lifetimes shorter than τ_{max} ($\Gamma_p^{-1} < \tau_{\text{max}}$) form a continuum. This spectral structure of relaxons resembles that of optical excitations of a hydrogen atom or of semiconductors (discrete excitons and a continuum) [69], although the former corresponds to inverse lifetimes while the latter correspond to energies. Also, we find that the effective velocity and Berry curvature scale as $\mathcal{O}(1)$ and $\mathcal{O}(1/\sqrt{N_k})$ for the discrete and continuum relaxons, respectively. This scaling, combined with the $\mathcal{O}(1)$ ($\mathcal{O}(N_k)$) scaling of the number of discrete (continuum) relaxons and the $\mathcal{O}(1)$ scaling of the relaxon lifetimes, makes the sum over relaxons in Eq. (6) convergent. As one increases the density of the k-point grid, the cumulative contribution remains discontinuous in the discrete regime and converges to a smooth curve in the continuum regime. See Sec. B and Fig. S2 of the Supplemental Material for details [35].

In Fig. 3, among the contributions of more than 10 000 relaxons to the conductivities, those of the two discrete, long-lived relaxons labeled “valley relaxon” and “minivalley relaxon” stand out. Remarkably, although these two relaxons contribute only 4% to the linear conductivity, they account for 37% of the NLH conductivity. We have named these relaxons based on their eigenstates shown in Fig. 4. The valley relaxon has a strong valley-polarizing character, describing the transfer of hole carriers from one valley to another valley. Similarly, the minivalley relaxon has a minivalley-polarizing character, in which “minivalley” refers to each of the two peaks of the Mexican-hat-like band structure within a single valley [Fig. 4(b)].

The eigenvectors of the valley and minivalley relaxons are peaked around the valence band maxima, with the same

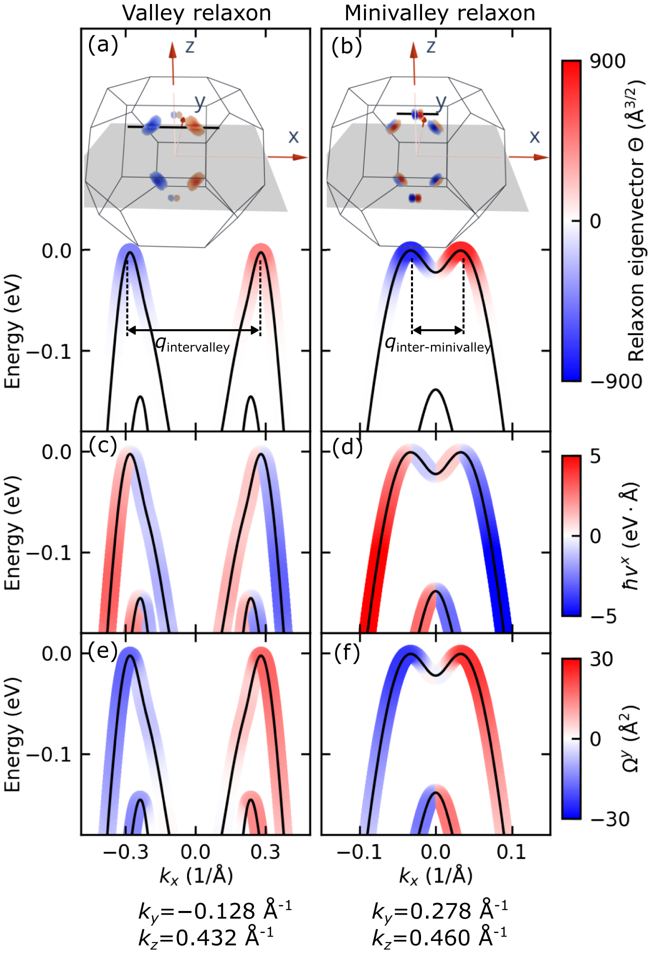

FIG. 4. Relaxon eigenvectors, velocity, and Berry curvature of GeTe. (a),(b) Relaxon eigenvector [Θ_{ip} in Eq. (5)]. (c),(d) Electron band velocity. (e),(f) Electron Berry curvature, along the solid black line in the inset of (a),(b). Inset: momentum-space distribution of the relaxon at the highest-energy valence band. The gray shading indicates the xy plane.

sign within a (mini)valley and the opposite signs between different (mini)valleys. Owing to the quadratic dispersion, the band velocities around the valence band maxima are small and approximately antisymmetric in wave vector space within a (mini)valley [Figs. 4(c) and 4(d)]. Hence, the effective velocity of the (mini)valley relaxons is low. In contrast, the Berry curvature is large near the valence band maxima and has the same parity in momentum space as the relaxon eigenvector [Figs. 4(e) and 4(f)]. Thus, both the valley and minivalley relaxons strongly couple to the Berry curvature, resulting in their large contribution to the NLH effect. This valley-polarization induced NLH effect will be present in all inversion-asymmetric materials with multiple valleys, such as the two-dimensional transition metal dichalcogenides [70].

The frequency dependence of the current responsivity [Fig. 2(b)] can be understood from the long lifetimes of the valley-polarizing relaxons, which originate from the weak intervalley scattering. Each relaxon gives a Drude-like contribution to the ac conductivity: a Lorentzian with a width Γ_p. Since the long-lived valley and minivalley relaxons contribute much more to the NLH conductivity than to the linear conductivity, the ac spectrum of the former is more sharply peaked at $\omega = 0$ than the latter. Hence, the current responsivity rapidly decays at higher frequencies as the contribution from the valley-polarizing relaxons decays faster than the remainder. Terahertz measurements could experimentally confirm this prediction.

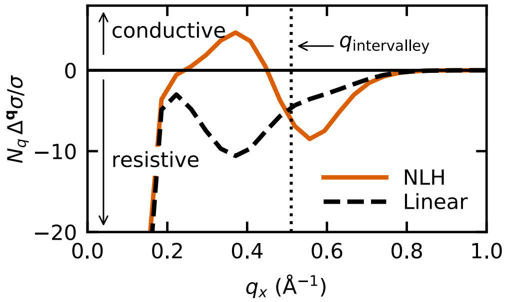

FIG. 5. Scattering diagnostics for GeTe along $\mathbf{q} = (q_x, 0, 0)$. $q_{\text{intervalley}}$ is the intervalley distance [Fig. 4(a)].

It may be surprising that the valley and minivalley relaxons are highly populated in the steady state under a uniform electric field, since a pure valley polarization by itself does not generate electric currents or couple to the electric field. In fact, the valley polarization vanishes in the CRTA because δf becomes a k derivative of the equilibrium occupation, whose integral over a valley is zero. The emergence of valley polarization is a result of the interplay of multiple intervalley scattering channels, as shown in a study of twisted bilayer graphene using a model with two circular Fermi surfaces and scattering matrix elements that vary sinusoidally with the electron wave vector direction [71].

To study which phonon modes contribute to the valley polarization, we propose and apply the "scattering diagnostics" method. We solve a modified BTE in which phonons with momentum $\mathbf{q}$ are excluded in the construction of the scattering matrix and see the change in conductivity, $\Delta^{\mathbf{q}}\sigma$, as we add back the missing scattering, i.e., recover the conductivity σ (see Sec. D of the Supplemental Material for details [35]). A negative value of $\Delta^{\mathbf{q}}\sigma/\sigma$ indicates that the scattering tends to suppress the conductivity, while a positive value indicates that the scattering enhances the conductivity, which would be an uncommon situation.

Figure 5 shows the scattering diagnostics for q points along the field direction. For the linear conductivity, $\Delta^{\mathbf{q}}\sigma$ is always negative, indicating that all scattering is resistive. In contrast, for the NLH effect, phonons with momentum close to but below the intervalley distance $q_{\text{intervalley}}$ increase the NLH conductivity. This behavior can be understood in terms of a four-state model (Fig. S6), which shows that large valley polarization can occur when the intervalley scattering rate is highly momentum dependent. For GeTe, the intervalley scatterings with momentum smaller than the intervalley distance, $q \lesssim q_{\text{intervalley}}$, are stronger than those with momentum larger than the intervalley distance, $q \gtrsim q_{\text{intervalley}}$. Scattering by phonons with $q \lesssim q_{\text{intervalley}}$ ($q \gtrsim q_{\text{intervalley}}$) strengthens (weakens) this momentum dependence, thus enhancing (suppressing) the valley polarization and the NLH effect.

A similar analysis could be performed for the minivalley relaxons, based on the momentum dependence of the interminivalley scattering. The presence of minivalleys is a result of the Mexican-hat-like band structure of GeTe. We expect that the minivalley relaxon will also appear in other materials with a similar dispersion, such as the two-dimensional chalcogenides GaS, GaSe, and InSe [72–74].

Scattering-induced valley polarization is a general phenomenon that occurs in many polar and nonpolar semiconductors that have multiple valleys at momenta which are not time-reversal invariant (see Sec. E of the Supplemental Material for precise symmetry constraints [35]). The valley polarizability, valley polarization per current, of four common semiconductors, diamond, silicon, GaP, and AlSb, are all of similar order of magnitude to that of GeTe (Fig. S7).

Recently, Ref. [7] reported that the vertex correction to the intrinsic NLH conductivity is negligible for the toy model of two-dimensional Dirac electrons with a single valley and an isotropic scattering mechanism. Our first-principles study suggests that real materials would instead exhibit a substantial vertex correction when the detailed electronic structure with multiple (mini)valleys and momentum-dependent electron-phonon scattering is taken into account. Finding materials with multiple valleys and momentum-dependent scattering represents a new design principle for maximizing NLH efficiency.

The scattering-induced valley polarization affects not only the NLH effect, but also all observables that couple to the valley degree of freedom. Such observables include the spin polarization [75], orbital magnetization [76], and circular dichroism [77]. The interplay of the valley-polarizing relaxons with these degrees of freedom is an interesting direction for valleytronics research [78]. For example, circularly polarized luminescence [79,80] could be used to directly measure the valley-polarizing relaxons.

Moreover, our work shows that solving the full BTE and performing the relaxon analysis is a computationally tractable way to reveal emergent long-lived quantities in electronic dynamics and study how they affect the nonlinear responses. By combining the relaxon analysis and the theories of nonlinear transport including band-geometric effects [7,9,81–83] using *ab initio* scattering matrices [84,85], one can reveal novel response properties of real materials beyond the RTA, as demonstrated in this work for the NLH effect.

This work was supported by the Creative-Pioneering Research Program through Seoul National University, Korean NRF No-2023R1A2C1007297, and the Institute for Basic Science (No. IBSR009-D1). Computational resources have been provided by KISTI (KSC-2021-CRE-0573).

---

[*] jaemo.lihm@gmail.com
[†] cheolhwan@snu.ac.kr

[1] E. Deyo, L. E. Golub, E. L. Ivchenko, and B. Spivak, Semiclassical theory of the photogalvanic effect in non-centrosymmetric systems, arXiv:0904.1917v1.

[2] I. Sodemann and L. Fu, Quantum nonlinear Hall effect induced by Berry curvature dipole in time-reversal invariant materials, Phys. Rev. Lett. **115**, 216806 (2015).

[3] J. E. Moore and J. Orenstein, Confinement-induced Berry phase and helicity-dependent photocurrents, Phys. Rev. Lett. **105**, 026805 (2010).

[4] Q. Ma, S.-Y. Xu, H. Shen, D. MacNeill, V. Fatemi, T.-R. Chang, A. M. Mier Valdivia, S. Wu, Z. Du, C.-H. Hsu *et al.*, Observation of the nonlinear Hall effect under time-reversal-symmetric conditions, Nature (London) **565**, 337 (2019).

[5] K. Kang, T. Li, E. Sohn, J. Shan, and K. F. Mak, Nonlinear anomalous Hall effect in few-layer $\mathrm{WTe_2}$, Nat. Mater. **18**, 324 (2019).

[6] Z. Z. Du, H.-Z. Lu, and X. C. Xie, Nonlinear Hall effects, Nat. Rev. Phys. **3**, 744 (2021).

[7] Z. Z. Du, C. M. Wang, H.-P. Sun, H.-Z. Lu, and X. C. Xie, Quantum theory of the nonlinear Hall effect, Nat. Commun. **12**, 5038 (2021).

[8] S. Sinha, P. C. Adak, A. Chakraborty, K. Das, K. Debnath, L. V. Sangani, K. Watanabe, T. Taniguchi, U. V. Waghmare, A. Agarwal *et al.*, Berry curvature dipole senses topological transition in a moiré superlattice, Nat. Phys. **18**, 765 (2022).

[9] O. Matsyshyn and I. Sodemann, Nonlinear Hall acceleration and the quantum rectification sum rule, Phys. Rev. Lett. **123**, 246602 (2019).

[10] J. I. Facio, D. Efremov, K. Koepernik, J.-S. You, I. Sodemann, and J. van den Brink, Strongly enhanced Berry dipole at topological phase transitions in bitei, Phys. Rev. Lett. **121**, 246403 (2018).

[11] D. Kumar, C.-H. Hsu, R. Sharma, T.-R. Chang, P. Yu, J. Wang, G. Eda, G. Liang, and H. Yang, Room-temperature nonlinear Hall effect and wireless radiofrequency rectification in Weyl semimetal $\mathrm{TaIrTe_4}$, Nat. Nanotechnol. **16**, 421 (2021).

[12] H. Isobe, S.-Y. Xu, and L. Fu, High-frequency rectification via chiral Bloch electrons, Sci. Adv. **6**, eaay2497 (2020).

[13] C. Guo, Y. Hu, G. Chen, D. Wei, L. Zhang, Z. Chen, W. Guo, H. Xu, C.-N. Kuo, C. S. Lue, X. Bo, X. Wan, L. Wang, A. Politano, X. Chen, and W. Lu, Anisotropic ultrasensitive $\mathrm{PdTe_2}$-based phototransistor for room-temperature long-wavelength detection, Sci. Adv. **6**, eabb6500 (2020).

[14] Y. Zhang and L. Fu, Terahertz detection based on nonlinear Hall effect without magnetic field, Proc. Natl. Acad. Sci. U.S.A. **118**, e2100736118 (2021).

[15] N. D. Mermin, Lindhard dielectric function in the relaxation-time approximation, Phys. Rev. B **1**, 2362 (1970).

[16] G. D. Mahan, *Many-Particle Physics*, 3rd ed. (Kluwer Academic/Plenum Publishers, New York, 2000).

[17] A. Cepellotti, G. Fugallo, L. Paulatto, M. Lazzeri, F. Mauri, and N. Marzari, Phonon hydrodynamics in two-dimensional materials, Nat. Commun. **6**, 6400 (2015).

[18] A. Mu, Z. Sun, and A. J. Millis, Optical conductivity of the two-dimensional Hubbard model: Vertex corrections, emergent Galilean invariance, and the accuracy of the single-site dynamical mean field approximation, Phys. Rev. B **106**, 085142 (2022).

[19] S. Kim, S. Woo, and H. Min, Vertex corrections to the dc conductivity in anisotropic multiband systems, Phys. Rev. B **99**, 165107 (2019).

[20] K. Výborný, A. A. Kovalev, J. Sinova, and T. Jungwirth, Semiclassical framework for the calculation of transport anisotropies, Phys. Rev. B **79**, 045427 (2009).

[21] C. Xiao, D. Li, and Z. Ma, Role of band-index-dependent transport relaxation times in anomalous Hall effect, Phys. Rev. B **95**, 035426 (2017).

[22] J.-J. Zhou and M. Bernardi, *Ab initio* electron mobility and polar phonon scattering in GaAs, Phys. Rev. B **94**, 201201 (R) (2016).

[23] S. Poncé, E. R. Margine, and F. Giustino, Towards predictive many-body calculations of phonon-limited carrier mobilities in semiconductors, Phys. Rev. B **97**, 121201(R) (2018).

[24] S. Poncé, W. Li, S. Reichardt, and F. Giustino, First-principles calculations of charge carrier mobility and conductivity in bulk semiconductors and two-dimensional materials, Rep. Prog. Phys. **83**, 036501 (2020).

[25] S. Poncé, F. Macheda, E. R. Margine, N. Marzari, N. Bonini, and F. Giustino, First-principles predictions of Hall and drift mobilities in semiconductors, Phys. Rev. Res. **3**, 043022 (2021).

[26] D. C. Desai, B. Zviazhynski, J.-J. Zhou, and M. Bernardi, Magnetotransport in semiconductors and two-dimensional materials from first principles, Phys. Rev. B **103**, L161103 (2021).

[27] R. Claes, G. Brunin, M. Giantomassi, G.-M. Rignanese, and G. Hautier, Assessing the quality of relaxation-time approximations with fully automated computations of phonon-limited mobilities, Phys. Rev. B **106**, 094302 (2022).

[28] J. Park, J.-J. Zhou, Y. Luo, and M. Bernardi, Predicting phonon-induced spin decoherence from first principles: Colossal spin renormalization in condensed matter, Phys. Rev. Lett. **129**, 197201 (2022).

[29] J. Park, Y. Luo, J.-J. Zhou, and M. Bernardi, Many-body theory of phonon-induced spin relaxation and decoherence, Phys. Rev. B **106**, 174404 (2022).

[30] R. J. Hardy, Phonon Boltzmann equation and second sound in solids, Phys. Rev. B **2**, 1193 (1970).

[31] A. Cepellotti and N. Marzari, Thermal transport in crystals as a kinetic theory of relaxons, Phys. Rev. X **6**, 041013 (2016).

[32] M. Simoncelli, N. Marzari, and A. Cepellotti, Generalization of Fourier's law into viscous heat equations, Phys. Rev. X **10**, 011019 (2020).

[33] A. Cepellotti, J. Coulter, A. Johansson, N. S. Fedorova, and B. Kozinsky, Phoebe: A high-performance framework for solving phonon and electron Boltzmann transport equations, J. Phys. Mater. **5**, 035003 (2022).

[34] J. M. Ziman, *Electrons and Phonons: The Theory of Transport Phenomena in Solids* (Oxford University Press, Oxford, 2001).

[35] See Supplemental Material at http://link.aps.org/supplemental/10.1103/PhysRevLett.132.106402, which includes Refs. [36–59], for the details of the BTE and relaxon formalism, additional computational results, and computational details.

[36] J. Zhou, B. Liao, B. Qiu, S. Huberman, K. Esfarjani, M. S. Dresselhaus, and G. Chen, *Ab initio* optimization of phonon drag effect for lower-temperature thermoelectric energy conversion, Proc. Natl. Acad. Sci. U.S.A. **112**, 14777 (2015).

[37] N. H. Protik and B. Kozinsky, Electron-phonon drag enhancement of transport properties from a fully coupled *ab initio* Boltzmann formalism, Phys. Rev. B **102**, 245202 (2020).

[38] D. Xiao, M.-C. Chang, and Q. Niu, Berry phase effects on electronic properties, Rev. Mod. Phys. **82**, 1959 (2010).

[39] S. S. Tsirkin, P. A. Puente, and I. Souza, Gyrotropic effects in trigonal tellurium studied from first principles, Phys. Rev. B **97**, 035158 (2018).

[40] O. Gunnarsson, T. Schäfer, J. P. F. LeBlanc, E. Gull, J. Merino, G. Sangiovanni, G. Rohringer, and A. Toschi, Fluctuation diagnostics of the electron self-energy: Origin of the pseudogap physics, Phys. Rev. Lett. **114**, 236402 (2015).

[41] J. Isberg, M. Gabrysch, J. Hammersberg, S. Majdi, K. K. Kovi, and D. J. Twitchen, Generation, transport and detection of valley-polarized electrons in diamond, Nat. Mater. **12**, 760 (2013).

[42] I. Maliyov, J. Park, and M. Bernardi, *Ab initio* electron dynamics in high electric fields: Accurate prediction of velocity-field curves, Phys. Rev. B **104**, L100303 (2021).

[43] P. Giannozzi *et al.*, Advanced capabilities for materials modelling with Quantum ESPRESSO, J. Phys. Condens. Matter **29**, 465901 (2017).

[44] D. R. Hamann, Optimized norm-conserving Vanderbilt pseudopotentials, Phys. Rev. B **88**, 085117 (2013).

[45] M. van Setten, M. Giantomassi, E. Bousquet, M. Verstraete, D. Hamann, X. Gonze, and G.-M. Rignanese, The PseudoDojo: Training and grading a 85 element optimized norm-conserving pseudopotential table, Comput. Phys. Commun. **226**, 39 (2018).

[46] J. P. Perdew, K. Burke, and M. Ernzerhof, Generalized gradient approximation made simple, Phys. Rev. Lett. **77**, 3865 (1996).

[47] J. Krempaský, H. Volfová, S. Muff, N. Pilet, G. Landolt, M. Radović, M. Shi, D. Kriegner, V. Holý, J. Braun, H. Ebert, F. Bisti, V. A. Rogalev, V. N. Strocov, G. Springholz, J. Minár, and J. H. Dil, Disentangling bulk and surface Rashba effects in ferroelectric α-GeTe, Phys. Rev. B **94**, 205111 (2016).

[48] G. Pizzi *et al.*, Wannier90 as a community code: New features and applications, J. Phys. Condens. Matter **32**, 165902 (2020).

[49] J. Bezanson, A. Edelman, S. Karpinski, and V. B. Shah, JULIA: A fresh approach to numerical computing, SIAM Rev. **59**, 65 (2017).

[50] IterativeSolvers.jl (v0.9.2), https://github.com/JuliaLinearAlgebra/IterativeSolvers.jl (2021).

[51] J.-M. Lihm and C.-H. Park, Comprehensive theory of second-order spin photocurrents, Phys. Rev. B **105**, 045201 (2022).

[52] X. Wang, J. R. Yates, I. Souza, and D. Vanderbilt, *Ab initio* calculation of the anomalous Hall conductivity by Wannier interpolation, Phys. Rev. B **74**, 195118 (2006).

[53] F. Macheda, P. Barone, and F. Mauri, Electron-phonon interaction and longitudinal-transverse phonon splitting in doped semiconductors, Phys. Rev. Lett. **129**, 185902 (2022).

[54] M. Royo and M. Stengel, First-principles theory of spatial dispersion: Dynamical quadrupoles and flexoelectricity, Phys. Rev. X **9**, 021050 (2019).

[55] G. Brunin, H. P. C. Miranda, M. Giantomassi, M. Royo, M. Stengel, M. J. Verstraete, X. Gonze, G.-M. Rignanese, and G. Hautier, Electron-phonon beyond Fröhlich: Dynamical quadrupoles in polar and covalent solids, Phys. Rev. Lett. **125**, 136601 (2020).

[56] V. A. Jhalani, J.-J. Zhou, J. Park, C. E. Dreyer, and M. Bernardi, Piezoelectric electron-phonon interaction from *ab initio* dynamical quadrupoles: Impact on charge transport in Wurtzite GaN, Phys. Rev. Lett. **125**, 136602 (2020).

[57] Brillouin.jl (v0.5.4), https://github.com/thchr/Brillouin.jl (2022).

[58] Interpolations.jl (v0.14.0), https://github.com/JuliaMath/Interpolations.jl (2022).

[59] V. Askarpour and J. Maassen, Unusual thermoelectric transport anisotropy in quasi-two-dimensional rhombohedral GeTe, Phys. Rev. B **100**, 075201 (2019).

[60] D. Di Sante, P. Barone, R. Bertacco, and S. Picozzi, Electric control of the giant Rashba effect in bulk GeTe, Adv. Mater. **25**, 509 (2013).

[61] A. H. Edwards, A. C. Pineda, P. A. Schultz, M. G. Martin, A. P. Thompson, and H. P. Hjalmarson, Theory of persistent, p-type, metallic conduction in c-GeTe, J. Phys. Condens. Matter **17**, L329 (2005).

[62] J. Li, Z. Chen, X. Zhang, H. Yu, Z. Wu, H. Xie, Y. Chen, and Y. Pei, Simultaneous optimization of carrier concentration and alloy scattering for ultrahigh performance GeTe thermoelectrics, Adv. Sci. **4**, 1700341 (2017).

[63] Z. Bu, W. Li, J. Li, X. Zhang, J. Mao, Y. Chen, and Y. Pei, Dilute Cu_2Te-alloying enables extraordinary performance of r-GeTe thermoelectrics, Mater. Today Phys. **9**, 100096 (2019).

[64] J. Dong, F.-H. Sun, H. Tang, J. Pei, H.-L. Zhuang, H.-H. Hu, B.-P. Zhang, Y. Pan, and J.-F. Li, Medium-temperature thermoelectric GeTe: Vacancy suppression and band structure engineering leading to high performance, Energy Environ. Sci. **12**, 1396 (2019).

[65] C. Verdi, F. Caruso, and F. Giustino, Origin of the crossover from polarons to Fermi liquids in transition metal oxides, Nat. Commun. **8**, 15769 (2017).

[66] M. Fiorentini and N. Bonini, Thermoelectric coefficients of n-doped silicon from first principles via the solution of the Boltzmann transport equation, Phys. Rev. B **94**, 085204 (2016).

[67] F. Macheda and N. Bonini, Magnetotransport phenomena in p-doped diamond from first principles, Phys. Rev. B **98**, 201201(R) (2018).

[68] F. Macheda, S. Poncé, F. Giustino, and N. Bonini, Theory and computation of Hall scattering factor in graphene, Nano Lett. **20**, 8861 (2020).

[69] M. Cardona and Y. Y. Peter, *Fundamentals of Semiconductors* (Springer, New York, 2005), Vol. 619.

[70] K. F. Mak, K. L. McGill, J. Park, and P. L. McEuen, The valley Hall effect in MoS_2 transistors, Science **344**, 1489 (2014).

[71] X. Ying, M. Ye, and L. Balents, Current switching of valley polarization in twisted bilayer graphene, Phys. Rev. B **103**, 115436 (2021).

[72] D. V. Rybkovskiy, A. V. Osadchy, and E. D. Obraztsova, Transition from parabolic to ring-shaped valence band maximum in few-layer GaS, GaSe, and InSe, Phys. Rev. B **90**, 235302 (2014).

[73] I. A. Kibirev, A. V. Matetskiy, A. V. Zotov, and A. A. Saranin, Thickness-dependent transition of the valence band shape from parabolic to Mexican-hat-like in the MBE grown InSe ultrathin films, Appl. Phys. Lett. **112**, 191602 (2018).

[74] W. Li, S. Poncé, and F. Giustino, Dimensional crossover in the carrier mobility of two-dimensional semiconductors: The case of InSe, Nano Lett. **19**, 1774 (2019).

[75] D. Xiao, G.-B. Liu, W. Feng, X. Xu, and W. Yao, Coupled spin and valley physics in monolayers of MoS_2 and other group-VI dichalcogenides, Phys. Rev. Lett. **108**, 196802 (2012).

[76] D. Xiao, W. Yao, and Q. Niu, Valley-contrasting physics in graphene: Magnetic moment and topological transport, Phys. Rev. Lett. **99**, 236809 (2007).

[77] W. Yao, D. Xiao, and Q. Niu, Valley-dependent optoelectronics from inversion symmetry breaking, Phys. Rev. B **77**, 235406 (2008).

[78] J. R. Schaibley, H. Yu, G. Clark, P. Rivera, J. S. Ross, K. L. Seyler, W. Yao, and X. Xu, Valleytronics in 2D materials, Nat. Rev. Mater. **1**, 1 (2016).

[79] K. F. Mak, K. He, J. Shan, and T. F. Heinz, Control of valley polarization in monolayer MoS_2 by optical helicity, Nat. Nanotechnol. **7**, 494 (2012).

[80] H. Zeng, J. Dai, W. Yao, D. Xiao, and X. Cui, Valley polarization in MoS_2 monolayers by optical pumping, Nat. Nanotechnol. **7**, 490 (2012).

[81] D. E. Parker, T. Morimoto, J. Orenstein, and J. E. Moore, Diagrammatic approach to nonlinear optical response with application to Weyl semimetals, Phys. Rev. B **99**, 045121 (2019).

[82] T. Holder, D. Kaplan, and B. Yan, Consequences of time-reversal-symmetry breaking in the light-matter interaction: Berry curvature, quantum metric, and diabatic motion, Phys. Rev. Res. **2**, 033100 (2020).

[83] J. Ahn, G.-Y. Guo, N. Nagaosa, and A. Vishwanath, Riemannian geometry of resonant optical responses, Nat. Phys. **18**, 290 (2022).

[84] S. Poncé, E. Margine, C. Verdi, and F. Giustino, EPW: Electron–phonon coupling, transport and superconducting properties using maximally localized Wannier functions, Comput. Phys. Commun. **209**, 116 (2016).

[85] J.-J. Zhou, J. Park, I.-T. Lu, I. Maliyov, X. Tong, and M. Bernardi, PERTURBO: A software package for *ab initio* electron–phonon interactions, charge transport and ultrafast dynamics, Comput. Phys. Commun. **264**, 107970 (2021).